Advances in Geo-Energy Research

Vol. 20, No. 2, p. 180-193, 2026

Original article

A coupled flow-geomechanics model for fractured shale oil reservoirs constructed using the virtual element method

Guanglong Sheng[1,2,3], Zhibin Yi[1,2,4], Hui Zhao[1,2,3]*, Mingjing Lu[5], Tongyun Yao[6], Huiru Sun[7]

[1]*School of Petroleum Engineering, Yangtze University, Wuhan 430100, P. R. China*

[2]*National Key Laboratory of Low-Carbon Catalysis and CO_2 Utilization, Yangtze University, Wuhan 430100, P. R. China*

[3]*Western Research Institute, Yangtze University, Karamay 834000, P. R. China*

[4]*Sinopec Jianghan Oilfield, Qianjiang 433100, P. R. China*

[5]*Shengli oil field exploration and Development Research Institute, Dongying 257000, P. R. China*

[6]*State Key Laboratory of Petroleum Resources and Engineering, China University of Petroleum, Beijing 102249, P. R. China*

[7]*Deep Earth Energy Laboratory, Department of Civil Engineering, Monash University, Melbourne VIC 3800, Australia*

Keywords:
Shale oil
flow-geomechanics coupling
virtual element method
coupled geomechanical model
sensitivity analysis

Cited as:
Sheng, G., Yi, Z., Zhao, H., Lu, M., Yao, T., Sun, H. A coupled flow-geomechanics model for fractured shale oil reservoirs constructed using the virtual element method. Advances in Geo-Energy Research, 2026, 20(2): 180-193.
https://doi.org/10.46690/ager.2026.05.06

Abstract:
The accurate prediction of shale oil production requires strong coupling between flow and geomechanics. However, traditional models often overlook the dynamic permeability damage induced by *in-situ* stress variations. To address this issue, our study establishes a fully coupled numerical simulation framework based on the virtual element method. This framework directly employs unstructured polyhedral grids generated by geological modeling software. This approach provides a distinct advantage over conventional methods, which rely on mesh reconstruction and exhibit severe distortion problems under large deformations. The model is validated using production data from a real field block, demonstrating the ability to accurately reproduce complex flow regime transitions and stress-induced production decline. Quantitative analysis identifies the Biot modulus as a key parameter governing reservoir stress sensitivity. Lower modulus values directly lead to substantial and sustained permeability damage. High fracture conductivity provides an initial productivity enhancement; however, it also accelerates stress redistribution around fractures that can cause severe localized permeability impairment in the vicinity of fracture roots over a relatively short production period. This work establishes a new integrated simulation model that couples geomechanical feedback with fluid flow, providing a quantitative engineering basis for effectively optimizing pressure-controlled production strategies and hydraulic fracturing design in shale oil reservoirs.

1. Introduction

Shale oil is a crucial unconventional resource in the global energy transition, and its exploration and development have become a central focus. Shale reservoirs feature a dense structure and ultra-low permeability, which makes commercial production rely heavily on large-scale hydraulic fracturing (Park et al., 2021; Huang et al., 2024; You et al., 2025). After fracturing, a complex network of pre-existing natural fractures and induced hydraulic fractures forms. Song et al. (2024) asserted that shale oil reservoirs exhibit fundamentally different fluid phase behavior and nonlinear flow mechanisms under nanoconfinement, posing major challenges to traditional simulation methods that assume a rigid porous medium. The fracture network displays distinct multi-scale characteristics

Yandy Scientific Press

*Corresponding author.
E-mail address: shenggl2019@yangtzeu.edu.cn (G. Sheng); 2023710316@yangtzeu.edu.cn (Z. Yi); zhaohui@yangtzeu.edu.cn (H. Zhao); mingjinglu2021@163.com (M. Lu); yaotongyun@student.cup.edu.cn (T. Yao); huiru.sun@monash.edu (H. Sun).
2207-9963
Received March 19, 2026; revised April 17, 2026; accepted May 6, 2026; available online May 10, 2026.

and strong heterogeneity, creating a unique structure that leads to flow mechanisms that differ fundamentally from those in conventional reservoirs, with significant anisotropy and pronounced stress sensitivity (Fernandes et al., 2019; Micheal et al., 2021). During production, continuous fluid extraction causes pore pressure to decline gradually. The pressure drop induces a redistribution of effective stress that deforms the rock skeleton, closes nano- and micro-scale pores, and reduces fracture conductivity, with these effects further restricting fluid flow. The strong coupling between the seepage field and the stress field greatly increases the uncertainty in productivity prediction (Zhang et al., 2022; Wu et al., 2023). Therefore, neglecting this fluid-solid coupling effect can lead to significant production forecast deviations (Shen et al., 2022; Hu et al., 2024), and accurately understanding fluid migration and achieving precise forecasting require a model that characterizes the co-evolution of seepage and stress fields.

The academic community has conducted extensive foundational research on fluid-solid coupling. Terzaghi first proposed the effective stress concept, revealing the interaction between solid deformation and fluid flow (Cryer, 1963). Biot (1955) later extended this theory to three-dimensional space and established the three-dimensional consolidation theory, laying the theoretical foundation for modern seepage-stress coupling research. Based on this framework, many scholars introduced fluid-solid coupling into shale oil development. They proposed various mathematical models, including the equivalent continuous medium model, the dual-porosity model, and the discrete fracture model (Zhang et al., 2020; Li et al., 2022). For instance, Wu et al. (2023) developed a multiscale gas-water two-phase coupling model that effectively addresses some production forecasting challenges. To resolve displacement discontinuities across fracture surfaces, Niu et al. (2020) combined the embedded discrete fracture model with the extended finite element method.

Although these physical models have partially revealed the presence of coupling mechanisms, their numerical solution methods still face significant challenges when handling the complex geometries of shale fracturing. Mainstream numerical approaches include the finite element method, the finite difference method, and the finite volume method. When these methods are used to simulate deformation in high-stress regions around hydraulic fractures, they typically require a large number of structured grids to represent fracture shapes, causing serious problems in grid topological adaptability (Huang et al., 2024). Moreover, these methods mostly rely on orthogonal structured meshes and struggle with discontinuous displacements at fractures. The finite difference method usually uses structured rectilinear grids. This grid characteristic severely limits geometric flexibility, making it difficult to conform to highly irregular fracture network boundaries and complex fluid-solid problems. Overall, the finite difference method inevitably introduces geometric fitting errors in boundary treatments (Zhan et al., 2023; Maulindani et al., 2025). Meanwhile, the finite volume method inherently possesses conservation properties, though its requirement for mesh orthogonality and its dependence on interpolation algorithms for nodal data constrain the accuracy of stress transfer during fluid-solid coupling (Zhu et al., 2012; Tuković et al., 2013; Jin et al., 2019). In summary, existing numerical methods have not been able to achieve an optimal balance among the complex fracture network geometry, adaptability to unstructured grids, and accurate stress representation. Notably, earlier studies predominantly treated the matrix, natural fractures and hydraulic fractures as rigid bodies, and rarely examined the mechanical properties of nano-scale and micro-scale pores or their microscopic control over permeability evolution.

Recent research has increasingly focused on fluid-solid coupling in shale reservoirs. For instance, Qi et al. (2025) established a nonlinear seepage model that accounts for slip, diffusion and desorption, finding that cumulative production differs notably when coupling is considered. Zhang et al. (2024) developed coupled flow-geomechanics models incorporating multiple mechanisms and emphasized the influence of complex fracture geometry on stress evolution. Xu et al. (2025) further reported that neglecting multi-physical coupling significantly overestimates gas distribution. Wang (2023) demonstrated the strong effect of temperature fields on fracture propagation, while Yao et al. (2025) achieved large-scale parallel coupling simulations on grids with hundreds of millions of elements. Despite these advances, however, existing methods still struggle with unstructured polyhedral grids and complex fracture networks under large deformation, facing mesh reconstruction difficulties, geometric fitting errors, and limited capacity to capture displacement discontinuities.

To overcome the above limitations, the virtual element method (VEM) offers a promising alternative. It supports arbitrary polyhedral elements without requiring explicit basis function integration, rather relying on energy decomposition and local projection (Xu et al., 2024). This inherent mesh adaptability avoids regeneration issues during large deformation. Thus, this paper establishes a VEM based fluid-solid coupling framework for shale fracturing. The framework directly imports complex fracture geometries, eliminating geometric errors and mesh reconstruction while dynamically updating physical properties to quantify how effective stress reduces fracture conductivity and matrix permeability.

The contributions of this study involve three main aspects. First, it provides a coupling framework with unstructured polyhedral meshes for accurately representing complex fracture geometries. Second, it investigates nano- and micro-pore stress sensitivity, clarifying how pore size controls permeability decline and how pore-throat deformation affects macroscopic productivity. Third, it systematically reveals how key fracturing and production parameters govern stress redistribution and permeability dynamics, highlighting distinct stress states near fracture tips and wellbores that influence fracture closure.

2. Fluid-solid coupling model

2.1 Seepage models in the shale reservoir

2.1.1 Seepage governing equations

Fluid flow in reservoir porous media is governed by the Navier-Stokes equations, first formulated by Navier (1823) and later refined by Stokes (1845). For incompressible flow

through an infinitely long capillary of uniform cross-section, the momentum equation simplifies to:

$$\frac{\mu}{r}\frac{\partial}{\partial r}\left(r\frac{\partial v}{\partial r}\right)=\frac{\partial p}{\partial L} \tag{1}$$

where μ represents fluid viscosisty, r represents pore radius, v represents fluid velocity, and L is the length of the pore.

Shale reservoirs contain pore-throat structures at the nanometer scale, resulting in pronounced non-Darcy flow that significantly exceeds predictions from Darcy's law under low permeability and pore pressure. To incorporate these microscale effects efficiently, an apparent permeability concept is adopted and integrated into a dual-media model. Since shale oil transport in nano-confinement is dominated by wall slip and near-wall property changes rather than Knudsen diffusion, the present work omits the diffusion term and derives the apparent permeability from a stratified flow framework.

The pore fluid is divided into a bulk layer and a boundary layer of higher viscosity, and a slip length is introduced at the pore wall. The modified Navier-Stokes equations are solved with slip and interfacial continuity conditions, yielding the velocity profile and volumetric flow rate:

$$Q_s=\left(\frac{\pi r^4}{8\mu_{eff}}+\frac{\pi l_s r^3}{2\mu_{eff}}\right)\frac{\Delta p}{L} \tag{2}$$

where Q_s represents fluid flow rate in the pores of a single circular pipe, μ_{eff} represents the equivalent viscosity considering fluid stratification, and l_s denotes the slip length.

However, shale rocks do not consist of a single straight capillary. To extend the single-tube flow law to the rock scale, porosity and tortuosity must be introduced. Combining this with Darcy's equation yields the apparent permeability of shale:

$$k_{app}=\frac{\phi r^2}{8\tau^2\left[(\mu_{eff}-1)\dfrac{\delta}{r}+1\right]}\left(1+\frac{4l_s}{r}\right) \tag{3}$$

where k_{app} represents the apparent permeability, σ denotes the thickness of boundary layer; and τ denotes the tortuosity of the pore.

The governing equations for the dual-porosity system are provided in Eq. (2):

$$\begin{cases}\nabla\cdot\left[\sum\limits_l\left(\dfrac{k_{app,f}k_{r,l}}{\mu_l}\nabla p_f\right)\right]+\sum\limits_l q_{ml}+Q_{wl}=\dfrac{\partial(\phi_f\rho_l S_l^f)}{\partial t}, & \text{in fracture}\\ \nabla\cdot\left[\sum\limits_{l=o,w}\left(\dfrac{k_{app,m}k_{r,l}}{\mu_l}\nabla p_l^m\right)\right]-\sum\limits_{l=o,w} q_{ml}=\dfrac{\partial(\phi_m\rho_l S_l^m)}{\partial t}, & \text{in matrix}\end{cases} \tag{4}$$

where subscripts f and m denote the fracture and matrix systems; subscripts l denotes the phase of fluids; k_{app} denotes the apparent permeability tensor. ρ denotes the density of fluid, q_{ml} denotes the inter-porosity flow rate and Q_{wl} represents the well flow rate at performed point.

The inter-porosity flow rate is taken as proportional to the pressure difference through a shape factor λ (Barenblatt et al., 1960):

$$q_{ml}=\lambda\frac{\rho_l k_m k_{r,l}}{\mu_l}\left(p_m-p_f\right) \tag{5}$$

For the complex hydraulic fracture network, an equivalent continuum approach based on grid marking is employed. Polyhedral elements intersected by fractures are identified in the virtual element mesh and assigned high permeability and porosity, while the remaining elements retain the matrix properties. This strategy exploits the capability of VEM with arbitrary polyhedra, avoiding the construction of non-matching meshes or low-dimensional interface elements while capturing fracture control on fluid-solid coupling at the macroscopic scale. Wells are introduced as source/sink terms in the fracture equations using the Peaceman formula, linking the well flow rate to the bottomhole pressure and the local grid pressure (HosseiniMehr et al., 2020):

$$Q_{wl}=\sum_l\left[\frac{2\pi\cdot T_{l,eff}}{\rho_l\mu_l}\left(p_{wf}-p_l\right)\right] \tag{6}$$

where p_{wf} represents the bottomhole pressure of well and p_l is the pressure of phase l.

2.1.2 Numerical discretization of the seepage equation

To connect with the subsequent stress field solution based on the VEM, the seepage equations are transformed into their weak form, i.e., the weighted residual form. To convert the nonlinear transient partial differential equations describing the complex seepage processes in shale reservoirs into solvable algebraic equations, the finite volume method is used for spatial discretization, combined with a fully implicit scheme for time discretization.

For the continuity equation (Eq. (4)) of phase l in the fracture/matrix system, within the control domain (Ω) of fluid flow, its residual form can be expressed as:

$$R_l^f=\nabla\cdot\left[T_{app,l}^f\nabla p_l^f\right]+(q_{ml}+Q_{wl})-\frac{\partial\left(\phi_f\rho_l S_l^f\right)}{\partial t}=0 \tag{7}$$

where l denotes the fluid phase, $T_{app,\,l}^f$ denotes the effective conductivity tensor of fluid phase l, and S is the saturation of fluid.

Integrating the residual equation (Eq. (7)), the weak form of the seepage equation can be obtained as:

$$\begin{aligned}\int_\Omega\nabla\cdot\left[T_{app,l}^f\nabla p_l^f\right]\omega_l\,\mathrm{d}\Omega=&-\int_\Omega\left[T_{app,l}^f\nabla p_l^f\right]\cdot\nabla\omega_l\,\mathrm{d}\Omega\\&+\oint_{\partial\Omega}\omega_l\left(T_{app,l}^f\nabla p_l^f\right)\cdot\mathbf{n}\,\mathrm{d}S\end{aligned} \tag{8}$$

where $\mathbf{n}$ represents the outward normal vector on the boundary $\partial\Omega$, and ω_l is the weighting function that satisfies the boundary conditions.

The boundary integral term on the right-hand side is used to impose closed boundary conditions, while constant pressure boundary conditions are directly imposed on the pressure term p_l^f. Finally, the weak form of the seepage equation in the fracture and matrix system can be expressed as:

$$\begin{cases} \int_\Omega \left[\mathbf{T}^f_{app,l}\nabla p^f_l\right]\cdot\nabla\omega_l\,\mathrm{d}\Omega - \int_\Omega (q_{ml}+Q_{wl})\,\omega_l\,\mathrm{d}\Omega \\ \quad + \int_\Omega \dfrac{\partial(\phi_f\rho_l S^f_l)}{\partial t}\omega_l\,\mathrm{d}\Omega = \oint_{\partial\Omega}\omega_l\mathbf{v}^f_l\cdot\mathbf{n}\,\mathrm{d}S \\ \int_\Omega \left[\mathbf{T}^m_{app,l}\nabla p^m_l\right]\cdot\nabla\omega_l\,\mathrm{d}\Omega - \int_\Omega q_{ml}\omega_l\,\mathrm{d}\Omega \\ \quad + \int_\Omega \dfrac{\partial(\phi_f\rho_l S^m_l)}{\partial t}\omega_l\,\mathrm{d}\Omega = \oint_{\partial\Omega}\omega_l\mathbf{v}^m_l\cdot\mathbf{n}\,\mathrm{d}S \end{cases} \tag{9}$$

Using a fully implicit scheme, the weak form is discretized in space by approximating the surface integral as the sum of the normal flux between adjacent grids. The spatial term of the seepage equation can be expressed as:

$$\begin{aligned} &\lambda_{l,ij}T_{ij}\left(p_{l,i}-p_{l,j}\right)-\left(q_{ml,i}+Q_{wl,i}\right)\Delta V_i \\ &-\frac{\Delta V_i}{\Delta t}\left[\left(\phi_f\rho_l S^f_l\right)^{n+1}_i-\left(\phi_f\rho_l S^f_l\right)^{n}_i\right]=0 \end{aligned} \tag{10}$$

where ΔV_i represents the volume variation of the domain, i and j are the Voigt notation of vectors, and n represents the number of iterations.

2.2 Mechanical model of the shale reservoir

2.2.1 Stress field deformation model

In this study, the VEM is used for stress field modeling and solving. It allows the use of arbitrary polyhedral meshes without the need to explicitly construct shape functions within the elements, greatly enhancing the adaptability of the model to complex geological structures.

The porous elastic governing equations incorporating pore pressure are based on Biot's poroelasticity theory. It is assumed that the rock skeleton is an isotropic linear elastic material that is in a quasi-static equilibrium state. Considering the coupling effect of fluid pore pressure on the skeleton, the governing equations consist of the momentum conservation equation, the geometric equation, and the constitutive equation. In the solution domain Ω, the stress equilibrium equation is expressed as (Niu et al., 2020):

$$\nabla\cdot\boldsymbol{\sigma}+\mathbf{f}=0 \tag{11}$$

where $\boldsymbol{\sigma}$ denotes the total stress tensor, and $\mathbf{f}$ is the body force vector.

Introducing the principle of effective stress, the relationship between the total stress, effective stress $\boldsymbol{\sigma}'$ and fluid pressure is given as follows (Niu et al., 2020):

$$\boldsymbol{\sigma}=\boldsymbol{\sigma}'-\alpha p\mathbf{I} \tag{12}$$

where α represents the Biot coefficient, and I is the second-order identity tensor.

Based on the principle of virtual work, for any virtual displacement $\delta\mathbf{u}$ that satisfies the boundary conditions, its weak form can be expressed as the internal virtual strain energy equal to the external virtual work:

$$\int_\Omega \boldsymbol{\sigma}:\delta\boldsymbol{\varepsilon}\,\mathrm{d}\Omega=\int_\Omega \mathbf{f}\cdot\delta\mathbf{u}\,\mathrm{d}\Omega+\int_{\Gamma_t}\mathbf{t}\cdot\delta\mathbf{u}\,\mathrm{d}S \tag{13}$$

where the bilinear form $a(\mathbf{u},\ \delta\mathbf{u})$ represents the internal elastic strain energy, $\mathbf{u}$ represents the displacement field vector, $\mathbf{b}$ denotes the body force applied to the polyhedral element, and $\mathbf{t}$ is the surface force applied to the element surface.

2.2.2 Solving the stress field with the VEM

The VEM decomposes a virtual displacement field into a polynomial part and a non-polynomial higher-order residual part using a projection operator. The stiffness matrix is then constructed from the degree-of-freedom vector at the vertices of each polyhedral element and a boundary-integral-based projection. For discretization on arbitrary polyhedral meshes, the first-order polynomial displacement space of an element is orthogonally decomposed into a rigid-body motion component and a constant-strain component.

The VEM begins by decomposing an arbitrary virtual displacement field into a rigid-body motion part, a constant-strain part, and a non-polynomial higher-order residual. Two projection operators are defined to isolate the physically meaningful components. The constant-strain projection extracts the average strain from the element degrees of freedom $\mathbf{U}_E$ through a matrix $\mathbf{W}_c$ (Gain et al., 2014):

$$\hat{\boldsymbol{\varepsilon}}_c=\mathbf{W}_c\mathbf{U}_E \tag{14}$$

where $\mathbf{W}_c$ denotes the projection coefficient that maps the virtual function to constant strain, and $\mathbf{U}_E$ is the node displacements of element.

Applying the divergence theorem, $\mathbf{W}_c$ is computed solely from the boundary geometry:

$$\mathbf{W}_c=\frac{1}{|E|}\int_{\partial E}\left(\mathbf{N}_c\mathbf{n}\right)^T\mathbf{N}_c\,\mathrm{d}S \tag{15}$$

where $\mathbf{N}_c$ represents the matrix that relates the nodal degrees of freedom to the constant-strain component. A rigid-body motion projection matrix $\mathbf{W}_r$ is similarly introduced, which maps $\mathbf{U}_E$ to the rigid-body coefficient vector $\mathbf{r}$ via a least-squares fit. The corresponding geometry matrix $\mathbf{N}_r$ describes the spatial distribution of the rigid-body basis. These two projections are combined into a total polynomial projection matrix $\mathbf{P}$ that returns the nodal values of the first-order polynomial part of the displacement (Gain et al., 2014):

$$\mathbf{U}_\pi=\mathbf{P}\mathbf{U}_E=\left(\mathbf{N}_r\mathbf{W}_r+\mathbf{N}_c\mathbf{W}_c\right)\mathbf{U}_E \tag{16}$$

Using this decomposition, the element stiffness matrix is built as the sum of a consistency term and a stabilization term. The consistency term preserves the elastic energy associated with the constant strain and is given by (Gain et al., 2014):

$$\mathbf{K}_\pi=|E|\mathbf{W}_c^T\mathbf{D}\mathbf{W}_c \tag{17}$$

where K_π represents the stiffness matrix of consistency term, $|E|$ denotes the volume of the elements, and $\mathbf{D}$ is the constitutive matrix.

Because the consistency term alone can produce rank deficiency, a stabilization term is added to control higher-order deformation modes and ensure positive definiteness (Gain et al., 2014):

$$\mathbf{K}_{stab}=\left(\mathbf{I}-\mathbf{P}\right)^T\mathbf{S}^E\left(\mathbf{I}-\mathbf{P}\right) \tag{18}$$

where $\mathbf{K}_{stab}$ represents the stiffness matrix of the stabilization

term, **I** denotes the identity matrix, and SE is the stabilization matrix that controls higher-order deformation modes in the VEM.

Gain et al. (2014) presented the construction of the stable matrix **S**, where the stiffness matrix of VEM is:

$$\mathbf{K}_E = |E|\mathbf{W}_c^T\mathbf{D}\mathbf{W}_c + (\mathbf{I}-\mathbf{P})^T\mathbf{S}(\mathbf{I}-\mathbf{P}) \tag{19}$$

External loads are discretized by projecting body forces and surface tractions onto the nodal degrees of freedom. According to the study of Andersen et al. (2017), the body force term ($\mathbf{F}_f$) becomes:

$$\mathbf{F}_f = \int_E \mathbf{N}^T\mathbf{N}_r\mathbf{W}_r^T\,\mathrm{d}\Omega\mathbf{f} \tag{20}$$

The surface traction term ($\mathbf{F}_t$) is integrated over the Neumann boundary using the boundary shape functions as (Andersen et al., 2017):

$$\mathbf{F}_t = \int_{\partial S} \mathbf{N}^T\mathbf{t}\,\mathrm{d}S \tag{21}$$

The fluid-solid coupling enters through the pore-pressure loading term ($\mathbf{F}_p$). After averaging the pressure over the element, the equivalent nodal force can be written as (Andersen et al., 2017):

$$\mathbf{F}_p = \int_\Omega \alpha p\nabla\cdot(\delta\mathbf{u})\,\mathrm{d}\Omega \tag{22}$$

where α denotes the Biot coefficient.

Following the standard finite element assembly procedure for stiffness matrices, the element contributions are assembled and the displacement boundary conditions are applied, which yields the global linear system:

$$\mathbf{K}\mathbf{U} = \mathbf{F}_f + \mathbf{F}_t + \mathbf{F}_p \tag{23}$$

Solving this system yields the reservoir displacement field. From the displacements, the strain and stress fields are computed through the constitutive law, and the updated stress state is fed back into the fluid-flow model, closing the coupling loop.

2.2.3 Seepage-stress coupling

Shale reservoir development involves strong nonlinear coupling between fluid flow in porous media and rock skeleton deformation. Pore pressure dissipation raises effective stress and compresses the skeleton, and the resulting volumetric strain reduces pore space and alters porosity and permeability, which in turn affects fluid flow. To capture this feedback, this study adopts a sequential iterative framework that dynamically updates the reservoir properties. In this framework, the element volumetric strain acts as the link between the stress and seepage fields. Using the constant strain projection operator of the VEM, the average volumetric strain of each element is directly computed from the nodal displacements.

Taking the derivation by Huang et al. (2025) as a basis, the porosity update model considering matrix compressibility is expressed as follows:

$$\phi = \frac{1}{1+\varepsilon_V}\left(\phi_0 + \alpha\varepsilon_V + \frac{1}{M}(p-p_0)\right) \tag{24}$$

where ϕ_0 represents the initial porosity, ε_V represents the current volumetric strain, M denotes the Biot modulus, and p and p_0 are the present reservoir pressure and initial pressure, respectively.

The Kozeny-Carman permeability model links permeability change to the cube of porosity change or volumetric strain, capturing tight-reservoir compressibility (Pei et al., 2024):

$$\frac{K}{K_0} = \frac{1}{1+\varepsilon_v}\left(1+\frac{\varepsilon_v}{\phi_0}\right)^3 \tag{25}$$

where K and K_0 represent the permeability at the current and initial time steps, respectively.

The effective stress increase closes the fracture surfaces and sharply reduces permeability as formation pressure depletes. This study uses the stress-sensitive model of Ren et al. (2019) to describe fracture conductivity changes during development:

$$k_f = \frac{k_{f0}}{\left[1+9\sigma_n/\sigma_{neff}\right]^2} \tag{26}$$

where k_{f0} represents the initial fracture permeability, σ_n is the e effective normal stress, and σ_{neff} is the effective stress when the fracture aperture is induced to 90%.

Shale oil reservoirs exhibit strong fluid-structure coupling. This paper uses the fixed-stress split scheme, which is a sequential iterative strategy. This method fixes the average total stress from the previous step while solving the flow equation, which decouples pressure and displacement and guarantees unconditional stability.

Specifically, in the k^{th} iteration at the $(n+1)^{\text{th}}$ time step, firstly, the volumetric strain of the solid skeleton $\varepsilon_v^{(k)} = \varepsilon_v^{(k-1)}$ is fixed and the modified pressure diffusion equation is solved to obtain the updated pressure field $p^{(k+1)}$. Subsequently, the updated pressure field is substituted into the mechanical equilibrium equation as the load, and the new displacement field $u^{(k+1)}$ and volumetric strain $\varepsilon^{(k+1)}$ are solved. This process is repeatedly iterated until the residuals of the pressure and displacement fields are less than the preset tolerances.

3. Model validation

To validate the model, the fluid-solid coupling stress solution is compared with that of Gudala and Govindarajan (2020). The computed displacement fields are compared, confirming the accuracy and feasibility of our method. In this case, the top boundary allows drainage and the other boundaries are fixed. Fig. 1 presents the validation results, which show that the VEM solution agrees well with the reference results. The vertical displacement comparison in Fig. 1 shows a close match, with an average error of 1.8%. Thus, applying VEM to coupled flow-stress problems in shale reservoir fracturing development is considered feasible.

The proposed model was compared with a black oil simulator and actual production data from the target block to evaluate its practicality and reliability. Fig. 2 displays the daily oil and water production rates from the model, the black oil model, and the actual data. The simulation results align well with the actual data over the entire production cycle, especially during

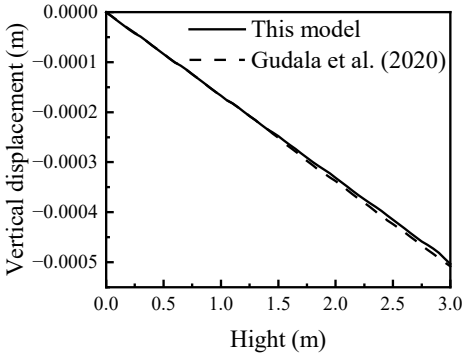

Fig. 1. Comparison of vertical displacement.

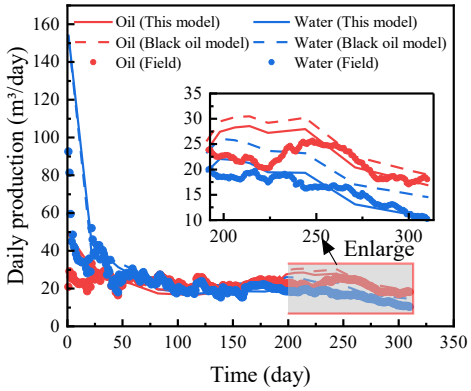

Fig. 2. Comparison of simulation results between the proposed model and the black oil model.

the late steady-state phase. The model accurately captures production fluctuations and stable trends, demonstrating its reliability in describing long-term flow behavior in the reservoir.

The traditional black oil model neglects geomechanical effects, while the proposed model provides better fitting results. For oil production, the black oil model overestimates steady-state production because it fails to capture the permeability reduction caused by declining formation pressure. In contrast, the proposed model quantifies the stress-sensitive decline in seepage capacity and reproduces a production decline trend that closely matches the actual data. For water production, the model also fits the actual data distribution better. This comparison highlights the need to account for the dynamic impact of stress changes on permeability and porosity in long-term shale reservoir simulations. Traditional black oil models ignore this key process and may overestimate the long-term capacity of the reservoir.

In conclusion, through comparisons with both the black oil model and actual production history, the VEM fully coupled model established in this study is shown to not only retain the advantages of traditional numerical methods for fluid flow calculations but also to improve production prediction accuracy by incorporating a geomechanics-coupled framework.

4. Influence of key parameters on the coupling model

This study analyzes the sensitivity of key geomechanical parameters to stress-field evolution and the dynamic permeability changes during shale reservoir production. For this purpose, a three-dimensional numerical model with dimensions of 150 m × 500 m × 33 m and a grid size of 1 m is selected. The model uses the same key geomechanical parameters as the validation part of the study, and it incorporates a single horizontal well with one fracturing stage divided into four perforation clusters. The stimulation creates a complex hydraulic fracture network; the primary fractures extend approximately 300 m from the wellbore. The aim is to clarify the multi-field coupling response mechanisms and provide a theoretical basis for optimizing development strategies. The sensitivity analysis adopts parameter values from the measured data of the target block or from typical ranges for this reservoir type. The geomechanical parameter ranges come from systematically organized triaxial compression test data of multiple coring wells in the target block, and the seepage parameter ranges are derived from logging interpretation statistics of the target block. Table 1 lists the parameters used for comparison and validation.

Table 1. List of key parameters of the model.

Parameter	Value
Young's modulus (GPa)	14.4
Poisson's ratio (-)	0.2
Biot's coefficient (-)	0.79
Oil density (kg/m^3)	940
Porosity (-)	0.2
Permeability (mD)	0.2

4.1 Impact of Biot modulus on productivity

Triaxial compression tests on cores from the target block yielded a Young's modulus mainly between 15 and 22 GPa. The sensitivity analysis therefore uses a range of 10 to 25 GPa, which covers the measured data and matches typical mechanical properties of this reservoir type, ensuring practical relevance. Other parameters, such as Poisson's ratio and the Biot coefficient, follow the same determination principle.

The Biot modulus controls the stress sensitivity of pore structure and thus directly influences permeability evolution. To quantify its effect on production, cumulative oil production under different modulus values was analyzed. Fig. 3 shows that cumulative oil production rises steadily as the Biot modulus increases. After one year of depletion, the low-modulus case (10 GPa) yields approximately 6.5% less cumulative oil than the high-modulus case (25 GPa). This indicates that, under the same production scheme, rock mechanical properties directly constrain ultimate recovery.

A rigid reservoir (high Biot modulus) experiences less elastic compression of pore space, which suppresses the closure of micro-nano pore throats and helps maintain higher porosity and flow channel volume. Consequently, the matrix retains higher permeability and supplies fluid continuously to the hy-

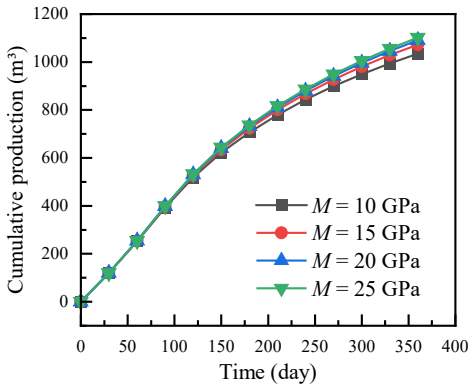

Fig. 3. Cumulative oil production under different Biot moduli.

draulic fractures. In a compliant reservoir (i.e., with low Biot modulus), pressure depletion causes significant compaction and pore volume reduction. This substantial deformation leads to marked permeability attenuation and severely impairs fluid transport. In ultra-low permeability shale reservoirs, permeability is the absolute bottleneck for production; the permeability damage caused by compaction in low-modulus rock outweighs any minimal energy release benefit. In contrast, high-modulus reservoirs keep more flow pathways open and deliver higher overall productivity.

The Biot modulus controls the pressure sensitivity of porosity and directly influences how fast effective stress builds up and how severely permeability deteriorates. As shown in Fig. 4(a), the effective stress increases steadily over time. After one year, the effective stress values for the low-modulus case (10 GPa) and the high-modulus case (25 GPa) are similar, both around 35.60 MPa, whereas the associated coupling effects differ considerably. A lower Biot modulus causes porosity to drop rapidly as pressure depletes, which accelerates microstructural contraction and intensifies stress concentration at grain contacts. A higher Biot modulus acts as a mechanical buffer and delays the accumulation of peak effective stress.

The effect on permeability evolution is more pronounced. Fig. 4(b) shows a clear separation among the normalized permeability curves for different modulus values. During the most severe damage phase, the permeability in the 10 GPa case declines to 0.9856. This reduction is 2.44 times greater than that for the 25 GPa case, highlighting a strong compaction sensitivity. In reservoirs with a low Biot modulus, the large reciprocal value causes pressure depletion to translate directly into severe pore volume compression, which leads to significant permeability loss that severely restricts later stage production. In contrast, reservoirs with a high Biot modulus possess stiffer pore structures; they effectively resist stress induced deformation and maintain permeability at a higher level.

In summary, the Biot modulus acts as a key control on pore structure stiffness and stress sensitivity. A lower modulus accelerates permeability degradation through stronger compaction; therefore, to avoid irreversible permeability damage, production drawdown should be carefully controlled in reservoirs with high compressibility.

4.2 Effect of porosity on productivity

This section quantitatively studies the governing mechanisms of porosity (0.07, 0.085, 0.1, 0.115) on production capacity, effective stress and permeability evolution at a fixed initial permeability.

The simulation results in Fig. 5 demonstrate that cumulative oil production increases monotonically with porosity. By the end of production, the high-porosity case ($\phi = 0.115$) yields 1185.38 m^3, while the low-porosity case ($\phi = 0.07$) yields 795.24 m^3. Quantitative analysis indicates that for every 0.015 increase in porosity, the cumulative production rises by approximately 11.5%. High-porosity zones essentially represent the sweet spots of the reservoir: They contain more fluid and exhibit better micro-connectivity early on. Therefore, accurately identifying and efficiently developing these high-porosity regions is critical for sustaining high production in shale oil exploration and development.

To evaluate the influence of porosity on stress distribution and permeability, the effective stress distribution after one year of depletion was examined. Fig. 6(a) shows that in the low-porosity reservoir ($\phi = 0.07$), the stress field is highly heterogeneous, with strong local concentrations reaching peak values above 34 MPa. When porosity increases to 0.115, the stress distribution becomes more uniform. The zones of high stress concentration shrink and weaken, and the overall stress level drops to between 31 and 33 MPa. This difference arises from the mechanical response of the pore structure. Low porosity implies a stiffer, denser rock matrix. Under the same pore pressure depletion, effective stress does not dissipate efficiently through pore deformation and instead concentrates at the fracture tips. In contrast, high-porosity reservoirs possess higher pore compressibility; they absorb and buffer the effective stress increase through greater pore volume contraction, producing a more homogeneous stress field.

As production continues, the rate of stress increase slows down and the curves flatten. Higher porosity reservoirs experience lower effective stress values. After about 300 days, the effective stress in the $\phi = 0.07$ case exceeds that in the $\phi = 0.115$ case by roughly 5 MPa, confirming the suppressive effect of high porosity on effective stress growth. Effective stress rises rapidly in the early stage and more slowly later. The early pressure drop mainly occurs in the near-well region where stress loading concentrates. Later, the pressure drop funnel extends outward and reduces the pressure gradient, which slows the effective stress increase.

In low-porosity reservoirs, high and heterogeneous stress causes two main problems. First, high effective stress compresses pores and fractures and sharply reduces permeability. Second, stress concentration can cause shear slip or proppant embedment and degrade fracture conductivity. These factors together severely limit long-term productivity. In contrast, high-porosity reservoirs with more uniform stress help reduce stress-sensitive damage and maintain stable flow paths. Therefore, for low-porosity, high-stiffness reservoirs, production pressure differentials must be managed to prevent irreversible permeability damage. Furthermore, fracturing designs should optimize proppant placement in high-stress regions to preserve

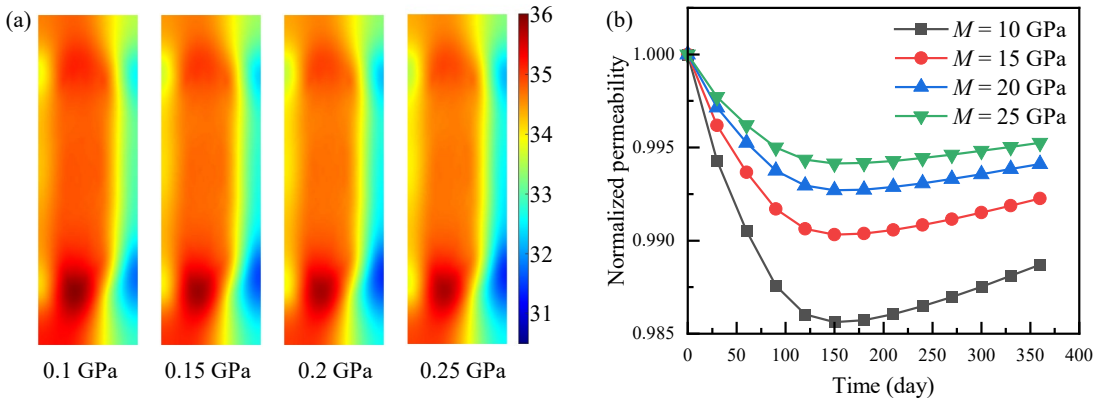

Fig. 4. Impact of Biot modulus on stress and permeability evolution: (a) Effective stress variation during production and (b) normalized permeability decline.

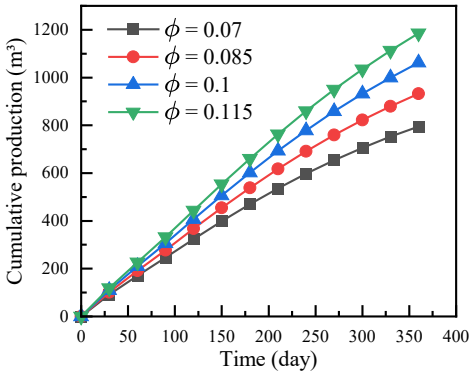

Fig. 5. Cumulative oil production under different porosities.

fracture effectiveness.

Porosity also strongly influences permeability evolution. To evaluate this effect, the normalized permeability trend was analyzed. Fig. 6(b) illustrates that the trend is not monotonic: Permeability declines initially and then undergoes a slight recovery. In early production, the rapid increase in effective stress compresses pore throats and natural fractures, causing an exponential drop in permeability. The low-porosity model, which accumulates effective stress faster, suffers the largest permeability loss, with the value falling to 99.31% of its initial level. Later in the production period, all models show a small permeability rebound. This counterintuitive behavior stems from matrix shrinkage under strong pressure depletion and the confinement of a closed boundary within the limited stimulated reservoir volume. As pore pressure drops, the elastic contraction of shale grains induces local tensile components that partially offset the earlier compressive stresses, reducing volumetric strain and slightly enhancing permeability.

In summary, porosity plays a dual role in shale oil production: It not only determines the initial volume of movable fluid but also governs the intensity of stress-seepage coupling. High porosity buffers effective stress growth through greater pore compressibility, yielding a more uniform stress field and imposing significantly less permeability damage. These effects make high-porosity zones a key geological control for sustaining long-term stable production.

4.3 Effects of nanopore size on productivity

This study simulated four typical pore radii (R = 25, 50, 75, 100 nm). Under the pressure differential within a high-conductivity fracture network, slight variations in microscale pore size are strongly amplified and exert a decisive influence on macroscale productivity. Minor changes in nanoscale pore size can significantly affect productivity by altering fluid occurrence states and flow resistance. The simulation results show a clear positive correlation between pore size and production performance. Fig. 7 presents the cumulative oil production curves. As the pore radius increases from 25 nm to 100 nm, the curves exhibit distinct tiered separation. By the end of production, the cumulative production for the 100 nm case is 12.5% higher than that for the 25 nm case.

Viscous resistance is the primary flow impediment in shale oil. Increasing the pore radius from 25 to 100 nm greatly reduces wall friction, which enhances fluid transport in the matrix and allows more fluid to be produced under the same pressure drop. Shale oil flow in nanopores also exhibits significant non-Darcy behavior. In very small pores (25 nm), the strong capillary forces and boundary layer effects prevent deep pressure propagation into the matrix. Under identical drawdown, larger pores (100 nm) achieve a greater pressure propagation radius and effectively access hydrocarbons farther from fractures; therefore, larger pores provide better flow pathways. More importantly, they expand the effective drainage volume, leading to substantially higher cumulative production. Nanopore size is not merely a storage property; it is a key factor controlling recoverability. Improving the pore structure decisively enhances productivity by lowering flow thresholds and reducing viscous resistance.

The evolution rate of the reservoir stress field correlates positively with pore size. Larger pores (R = 100 nm) allow faster fluid withdrawal, causing rapid pressure depletion and a greater effective stress increase near fractures. After one year, the effective stress in the R = 100 nm model reaches 36.20 MPa, significantly exceeding that in the R = 25 nm model. Fig. 8(a) shows the corresponding stress distribution. Under larger pore sizes, the stress concentration zone is more extensive and exhibits higher peak values, reflecting the elevated geomech-

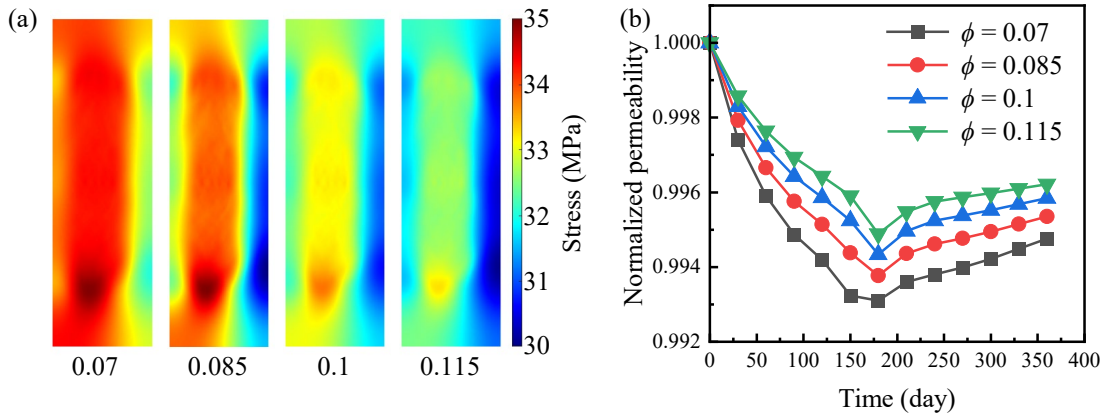

Fig. 6. Impact of porosity on stress distribution and permeability evolution: (a) Effective stress field after one year of depletion and (b) normalized permeability evolution.

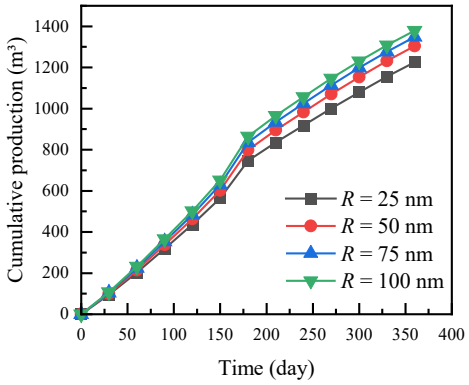

Fig. 7. Cumulative oil production under different pore radii.

anical risks that accompany high productivity. The areas of intense fluid extraction coincide with the most severe effective stress increase and structural damage.

Although the smaller pore model undergoes a lower total effective stress increase, it experiences more severe permeability loss, as shown in Fig. 8(b). In extremely small pores, a minor linear strain in the rock framework causes a large percentage reduction in the pore-throat flow area. Under the same stress, larger pores undergo a similar absolute contraction but a much smaller relative reduction. Consequently, smaller pores are more sensitive to external stress disturbances and display stronger stress-dependent permeability damage.

In summary, nanopore size plays a dual role: It governs fluid mobility and controls stress sensitivity. Larger pores enhance matrix supply capacity while keeping relative permeability loss modest, whereas smaller pores suffer disproportionately severe stress-induced damage. Pore size distribution is therefore a core control on both fluid availability and the extent of permeability impairment.

4.4 Impact of fracture conductivity on productivity and stress sensitivity

This section employs four typical fracture permeability values (0.1, 1, 10, and 100 D) to quantify their control on cumulative production, stress field evolution, and the degradation of fracture conductivity due to stress sensitivity.

Fig. 9 illustrates that production response to fracture conductivity falls into two distinct stages. In the low-conductivity stage, fracture flow capacity directly constrains productivity. Raising fracture permeability from 0.1 to 10 D increases one-year cumulative oil production by 11.5%, because higher conductivity reduces pressure loss along the fracture and expands the drainage area. In the high-conductivity stage, further increases bring diminishing returns. Raising the conductivity from 10 to 100 D adds only 3.2% to cumulative production. At this point, fracture transport capacity far exceeds the matrix supply, and productivity becomes matrix-limited.

This saturation effect originates from the extreme permeability contrast between the shale matrix and fractures. Once fracture conductivity surpasses a critical threshold (around 10 D in this study), the controlling mechanism shifts from fracture transport limitation to matrix supply limitation. Excess conductivity cannot be converted into additional production because the fluid supply is simply insufficient.

Higher conductivity reduces flow resistance within the fracture network. This accelerates fluid extraction near the wellbore, leading to rapid pore pressure depletion and a sharp increase in effective stress on the rock skeleton. After one year, the high-conductivity case (100 D) reaches an effective stress of 38.9 MPa, compared to 35.58 MPa for the low-conductivity case (0.1 D), with Fig. 10(a) showing the corresponding stress distribution. A high-stress concentration zone appears around high-conductivity fractures. The drained rock experiences higher closure stress and stronger stress heterogeneity, raising the risk of proppant and fracture face degradation.

The high-stress environment drives long-term fracture performance loss. Faster fluid withdrawal intensifies effective stress buildup, which compresses fracture width. The higher the conductivity, the stronger this feedback loop becomes, severely impairing flow efficiency over time. Fracture conductivity also controls how fast and how far matrix permeability declines by influencing pressure dissipation. Fig. 10(b) displays the normalized permeability evolution. In the early stage, the high-conductivity case shows a much faster permeability drop and earlier stabilization than the low-conductivity case. Stress sensitivity is therefore triggered more rapidly in high-

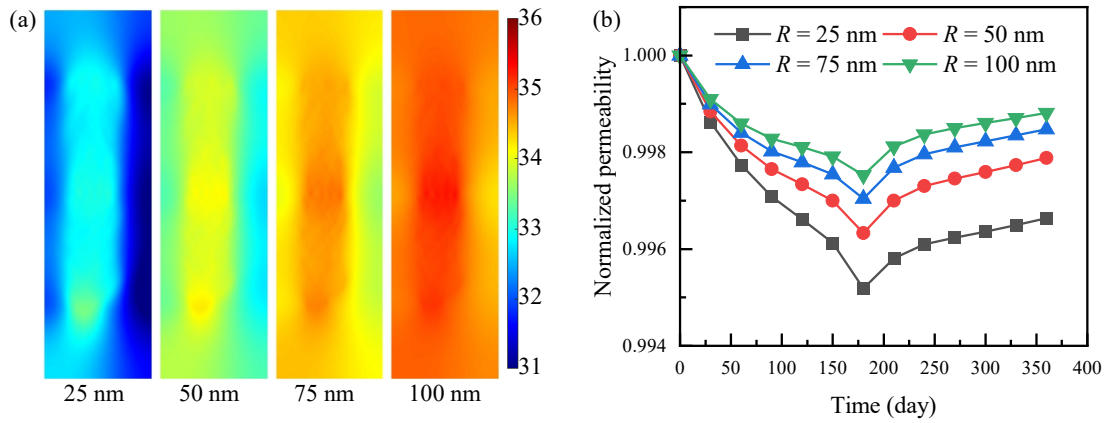

Fig. 8. Impact of pore radius on stress distribution and permeability evolution: (a) Stress field after one year of depletion and (b) normalized permeability decline.

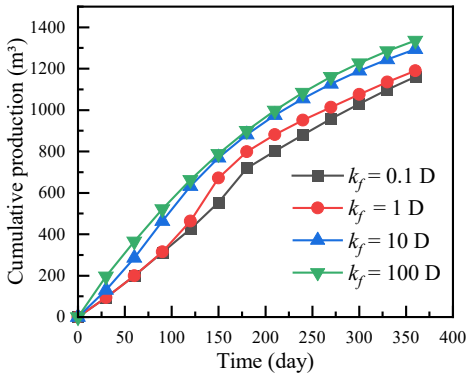

Fig. 9. Cumulative oil production under different pore radii.

conductivity fractures, causing quicker structural damage before pressure transients reach the boundary.

In summary, the benefit of fracture conductivity follows a clear pattern of diminishing returns. Moderate conductivity effectively expands the drainage area, whereas excessive conductivity initiates a negative feedback cycle of rapid depletion, high effective stress, and severe near-fracture permeability impairment. Fracture conductivity should therefore be matched to the matrix supply capacity, as this balance secures initial productivity while avoiding stress-induced damage that compromises long-term recovery.

5. Model application

This chapter applies the previously developed fluid solid coupling model and the insights from sensitivity analyses to a real block in a shale oil field. First, an unstructured grid model is built to match the actual geological characteristics. The study then conducts production history matching and productivity prediction, and also analyzes the temporal and spatial evolution of the reservoir stress field and seepage parameters during production. The aim is to verify the engineering applicability of the model and to guide field practice.

5.1 Geological modeling of the actual field

A three-dimensional geological model of the target block was built using Petrel software, which captures the complex geological structure and the multi-scale fracture network created by hydraulic fracturing. The model was then discretized with an unstructured polyhedral mesh suitable for VEM simulation. Unstructured meshes offer better geometric adaptability for complex boundaries and SRV regions than traditional structured corner-point grids. In addition, they avoid computational errors caused by grid distortion. The block model measures 1,290 m by 1,410 m, with an average thickness of 54 m. A horizontal well with 23 fracturing stages is placed along its lateral. To simulate post-fracturing flow accurately, hydraulic fractures are explicitly represented as high-conductivity pathways.

Model initialization is based on actual well log interpretations and rock mechanics test data from the target block. The simulation considers oil-water two-phase flow. The rock matrix is assumed to be an isotropic linear elastic material, and the analysis follows the small-deformation assumption. An overburden pressure of 5 MPa is applied at the top, with closed boundaries on the sides and bottom. The key reservoir property and geomechanical parameters are detailed in Table 2.

5.2 Production history matching and performance prediction

Production simulation and history matching were conducted using the unstructured grid geological model. Shale reservoir conditions are complex and uncertain, so a "parameter inversion-dynamic calibration" strategy was adopted. Actual field data on daily oil and water production rates guided the adjustment of key uncertain parameters, including hydraulic fracture conductivity, the matrix permeability stress-sensitivity coefficient, and fracture half-length.

The matching results are shown in Fig. 11. The simulated daily oil and water production rates from the coupled model agree well with field measurements. The model successfully captures the typical multi-stage flow-regime evolution during shale production and accurately reproduces the sharp decline in initial oil rate. As production continues, pressure propagates deeper into the matrix, and the flow mechanism shifts from fracture-dominated to coupled matrix-fracture flow. This close

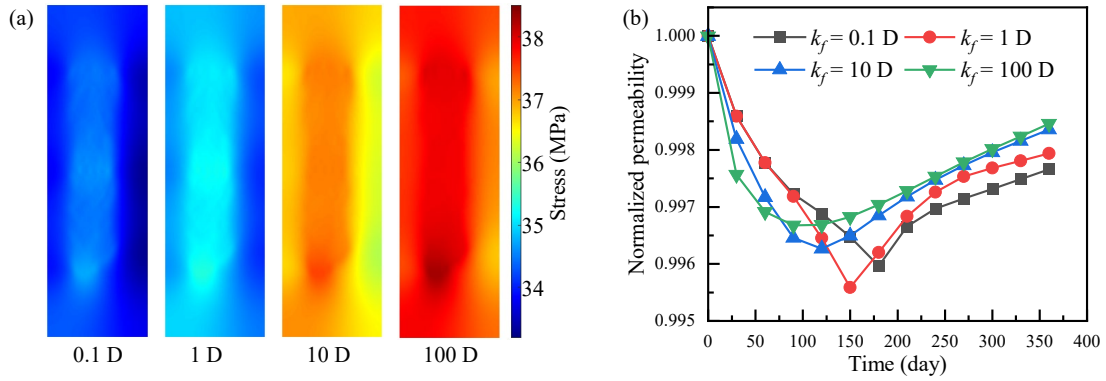

Fig. 10. Impact of fracture conductivity on stress and permeability: (a) Effective stress distribution after one year of production and (b) normalized permeability decline.

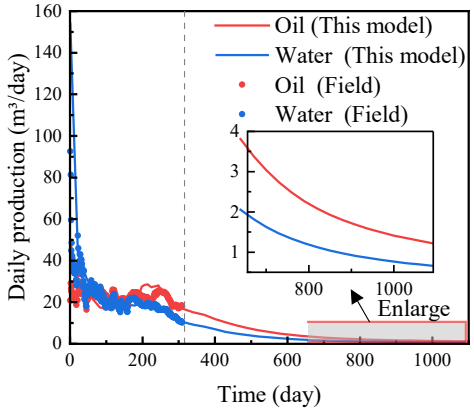

Fig. 11. Model history matching and production prediction results.

match validates the capability of the model to quantify the stress-permeability coupling mechanism.

After the high-precision history match, the ability of the model to characterize complex reservoir dynamics was verified, enabling an extrapolated forecast of future production trends. The simulation results indicate that as reservoir energy keeps depleting, the daily oil rate follows a typical hyperbolic decline and gradually stabilizes at a low plateau. This plateau directly reflects matrix deliverability becoming the dominant flow constraint. The accurate prediction is grounded in coupled geomechanical-fluid flow mechanisms, which confirms the reliability of the model in practical field applications and provides a solid basis for subsequent development decisions.

5.3 Dynamic reservoir evolution characteristics

This section analyzes the spatiotemporal evolution of subsurface multi-physical fields during shale oil depletion, providing quantitative insights into the complex fluid solid coupling mechanisms in tight reservoirs. As production proceeds and reservoir energy is released, the pressure and stress fields show strong interactive behavior. Pressure propagates radially from the high-conductivity hydraulic fractures into the low-permeability matrix, forming a characteristic pressure depletion funnel. Fig. 12 displays the pressure distribution at two key stages: Post-fracturing and after one year of production. In the latter case, the reservoir pressure has dropped by roughly

Table 2. Parameters of the shale reservoir injection depletion production model.

Parameter	Value
Average matrix permeability (mD)	0.102
Average matrix porosity (-)	0.101
Initial fracture porosity (-)	1
Young's modulus (GPa)	20.25
Poisson's ratio (-)	0.3
Biot's coefficient (-)	1
Fluid compressibility (MPa^{-1})	3.4×10^{-4}
Fluid viscosity (mPa·s)	2.76
Bottom hole pressure (MPa)	10
Average initial pore pressure (MPa)	56

13 MPa relative to the post-fracturing condition. The pressure decline concentrates mainly within the stimulated reservoir volume. Although the pressure-affected zone expands with time, the far-field pressure remains relatively high because the matrix permeability is extremely low.

Driven by poroelastic effects, the non-uniform pressure decline causes significant and heterogeneous redistribution of effective stress. Perpendicular to the fracture faces, rapid fluid withdrawal causes a sharp reduction in pore pressure. The matrix rock undergoes volumetric shrinkage, leading to a local decrease in the minimum horizontal stress. This stress redistribution is particularly obvious where fracture clusters are closely spaced, reflecting inter-fracture stress interference. After one year of production, the X-direction stress increases by approximately 6.5 MPa, the Y-direction stress by about 5 MPa, and the Z-direction stress by roughly 10 MPa. The vertical direction is mainly controlled by overburden gravity. As pore fluid is extracted, the loss of pore-pressure support raises the effective stress and compacts the reservoir. The resulting vertical subsidence at the surface and at the reservoir top reaches a maximum near the center of the fractured region, directly illustrating how fluid withdrawal drives deformation in the formation.

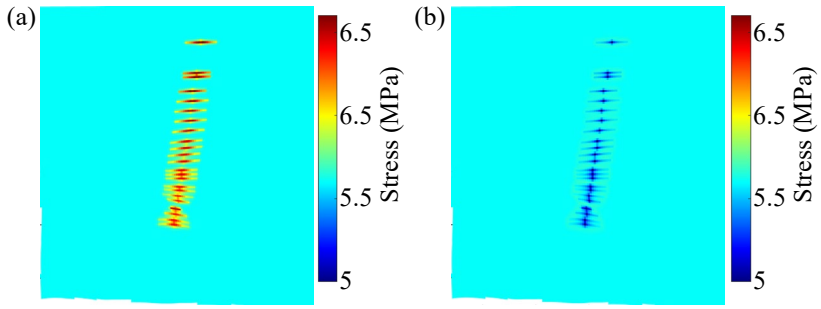

Fig. 12. Pressure distribution during shale oil production: (a) Post-fracturing and (b) after 1 year.

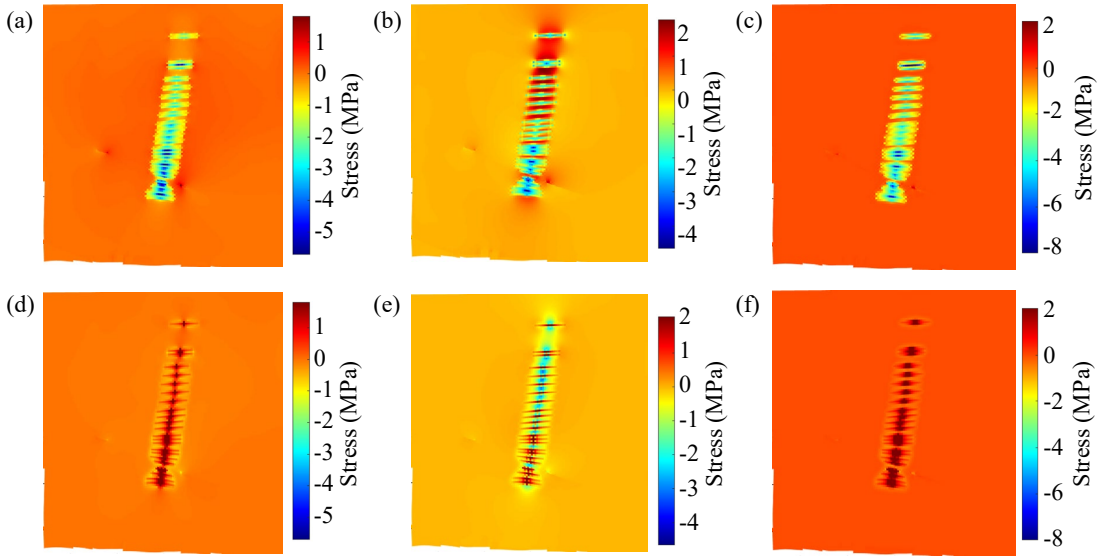

Fig. 13. Stress evolution in three orthogonal directions during production: (a) *X*-direction after fracturing, (b) *Y*-direction after fracturing, (c) *Z*-direction after fracturing, (d) *X*-direction after 1 year, (e) Y-direction after 1 year and (f) *Z*-direction after 1 year.

Permeability evolution is governed by stress sensitivity and exhibits complex spatiotemporal patterns. Fig. 14 shows the distribution of normalized permeability throughout the production lifecycle. Among them, Grids 1 and 5 are located at the tips of the fracture wings, Grids 2 and 4 are situated in the middle of the two fracture branches, and Grid 3 is at the fracture root. Permeability damage is highly concentrated near hydraulic fractures and within the SRV. Around fracture roots, flow velocity is high and pressure declines rapidly. The sharp effective-stress increase causes severe fracture closure, and the simulation shows that permeability in these zones can drop by more than 80% within two years. This becomes the primary source of increased flow resistance. In the matrix far from fractures, pressure changes are small, so permeability reduction is limited to about 10%. Near the fracture tips, permeability remains relatively stable in early production due to delayed pressure transmission.

6. Conclusions

In this study, a fully coupled fluid-structure simulation framework based on the VEM is developed for shale oil reservoirs with complex fracture networks. This framework uses unstructured polyhedral meshes, which can accurately capture the geometry of fracture networks and avoid mesh reconstruction under large deformations. Furthermore, it simulates the dynamic degradation of reservoir properties caused by strong stress sensitivity, overcoming the geometric and physical limitations of conventional methods. The proposed framework is validated with field production data, providing a quantitative tool for fracturing design and production optimization. The main findings are as follows:

1) Reservoir stress sensitivity is dominated by pore structure stiffness (Biot modulus). Low-modulus reservoirs experience stronger compaction and more severe permeability damage under pressure drop.
2) Fracture conductivity shows a diminishing marginal benefit on productivity. Beyond a critical value, the production gain becomes limited. Excessive conductivity intensifies stress accumulation and inter-fracture interference, which triggers a negative feedback that accelerates near-fracture permeability decline.
3) Permeability damage is highly heterogeneous and concentrates at the fracture roots.

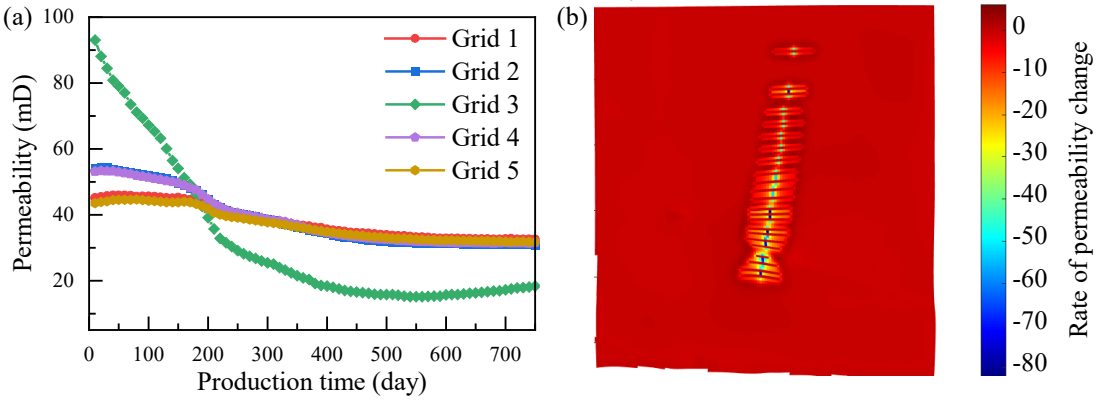

Fig. 14. Distribution of normalized permeability throughout the production lifecycle in shale oil fracturing development: (a) Permeability changes vs. time and (b) rate of change of permeability production.

Acknowledgements

This study was supported by the National Natural Science Foundation of China (Nos. 52474029 and 52525403), the National Natural Science Foundation of Hubei Province (No. 2026AFA086), the National Major Science and Technology Projects (No. 2024ZD1405105), the "Tianshan Talents" Training Program - Science and Technology Innovation Team Project of Xinjiang Uygur Autonomous Region (No. 2024TSYCTD0018).

Conflicts of interest

The authors declare no competing interest.

References

Andersen, O., Nilsen, H. M., Raynaud, X. Virtual element method for geomechanical simulations of reservoir models. Computational Geosciences, 2017, 21(5): 877-893.

Barenblatt, G. I., Zheltov, I. P., Kochina, I. Basic concepts in the theory of seepage of homogeneous liquids in fissured rocks. Journal of Applied Mathematics and Mechanics, 1960, 24(5): 1286-1303.

Biot, M. A. Theory of elasticity and consolidation for a porous anisotropic solid. Journal of Applied Physics, 1955, 26(2): 182-185.

Cryer, C. A comparison of the three-dimensional consolidation theories of Biot and Terzaghi. The Quarterly Journal of Mechanics and Applied Mathematics, 1963, 16(4): 401-412.

Fernandes, F. B., Campos, W., Braga, A. M. B., et al. Sensitivity analysis of the influence of fracturing spacing in the construction of complex fractures network for exploration and production of shale gas/shale oil. Journal of Petroleum & Environmental Biotechnology, 2019, 10: 397.

Gain, A. L., Talischi, C., Paulino, G. H. On the virtual element method for three-dimensional linear elasticity problems on arbitrary polyhedral meshes. Computer Methods in Applied Mechanics and Engineering, 2014, 282: 132-160.

Gudala, M., Govindarajan, S. K. Numerical modeling of coupled fluid flow and geomechanical stresses in a petroleum reservoir. Journal of Energy Resources Technology, 2020, 142(6): 063006.

HosseiniMehr, M., Vuik, C., Hajibeygi, H. Adaptive dynamic multilevel simulation of fractured geothermal reservoirs. Journal of Computational Physics: X, 2020, 7: 100061.

Hu, Y., Li, X., Zhang, Z., et al. A review on hydro-mechanical coupling simulations of hydraulic fracture network in shale reservoirs. Journal of Engineering Geology, 2024, 32(4): 1381-1396. (in Chinese)

Huang, L., Liao, X., Fan, M., et al. Experimental and numerical simulation technique for hydraulic fracturing of shale formations. Advances in Geo-Energy Research, 2024, 13(2): 83-88.

Huang, L., Zhan, W., Zhao, H., et al. A novel fluid-solid coupling method for fractured reservoirs: 3D DDM-EDFM integration with proppant mechanics. Computers and Geotechnics, 2025, 181: 107127.

Jin, P., Xie, B., Xiao, F. Multi-moment finite volume method for incompressible flows on unstructured moving grids and its application to fluid-rigid body interactions. Computers & Structures, 2019, 221: 91-110.

Li, H., Lei, H., Yang, Z., et al. A hydro-mechanical-damage fully coupled cohesive phase field model for complicated fracking simulations in poroelastic media. Computer Methods in Applied Mechanics and Engineering, 2022, 399: 115451.

Maulindani, S. F., Prima, A., Wibowo, J. A., et al. Numerical simulation study using the explicit finite difference method for petroleum reservoir. ComTech: Computer, Mathematics and Engineering Applications, 2025, 16(2): 53-168.

Micheal, M., Xu, W., Xu, H., et al. Multi-scale modelling of gas transport and production evaluation in shale reservoir considering crisscrossing fractures. Journal of Natural Gas Science and Engineering, 2021, 95: 104156.

Navier, C. L. Mémoire sur les lois du mouvement des flu-

ides. Mémoires de l'Académie Royale des Sciences de l'Institut de France, 1823, 6(1823): 389-440.

Niu, J., Su, J., Yan, X., et al. An efficient numerical simulation method with hydro-mechanical coupling model of fractured shale oil reservoir based on embedded discrete fracture model and extended finite element method. Science Technology and Engineering, 2020, 20(7): 2643-2651. (in Chinese)

Park, J., Iino, A., Datta-Gupta, A., et al. Novel hybrid fast marching method-based simulation workflow for rapid history matching and completion design optimization of hydraulically fractured shale wells. Journal of Petroleum Science and Engineering, 2021, 196: 107718.

Pei, X., Liu, Y., Lin, Z., et al. Anisotropic dynamic permeability model for porous media. Petroleum Exploration and Development, 2024, 51(1): 193-202.

Qi, Q., Yue, M., Zhu, W., et al. Fluid-solid coupling productivity analysis of multi-stage fractured horizontal wells in shale reservoirs. Chinese Journal of Engineering, 2025, 47(5): 1128-1136.

Ren, L., Su, Y., Zhan, S., et al. Fully coupled fluid-solid numerical simulation of stimulated reservoir volume (SRV)-fractured horizontal well with multi-porosity media in tight oil reservoirs. Journal of Petroleum Science and Engineering, 2019, 174: 757-775.

Shen, W., Ma, T., Li, X., et al. Fully coupled modeling of two-phase fluid flow and geomechanics in ultra-deep natural gas reservoirs. Physics of Fluids, 2022, 34(4): 043101.

Song, Y., Song, Z., Chen, Z., et al. Fluid phase behavior in multi-scale shale reservoirs with nano-confinement effect. Energy, 2024, 289: 130027.

Stokes, G. G. On the theories of the internal friction of fluids in motion, and of the equilibrium and motion of elastic solids. Transactions of the Cambridge Philosophical Society, 1845, 8(4): 75-129.

Tuković, Ž., Ivanković, A., Karač, A. Finite-volume stress analysis in multi-material linear elastic body. International Journal for Numerical Methods in Engineering, 2013, 93(4): 400-419.

Wang, L. Study on the influence of temperature on fracture propagation in ultra-deep shale formation. Engineering Fracture Mechanics, 2023, 281: 109-118.

Wu, J., Zhu, W., Zhang, D., et al. Non-grid numerical simulation of two-phase fluid-solid coupling for shale gas reservoir. Special Oil & Gas Reservoirs, 2023, 30(4): 96-103. (in Chinese)

Xu, B., Fan, W., Wriggers, P. High-order 3D virtual element method for linear and nonlinear elasticity. Computer Methods in Applied Mechanics and Engineering, 2024, 431: 117258.

Xu, F., Li, Y., Xu, X., et al. Thermal-hydrological-mechanical coupling simulation of matrix-type shale oil: Analysis of oil-gas-water multiphase flow mechanism under various parameter conditions. Geoenergy Science and Engineering, 2025, 246: 213656.

Yao, J., Wang, T., Sun, Z., et al. Massively parallel numerical simulation technology for thermo-hydro-mechanical coupling using general embedded discrete fracture model. Energy and Power Journals, 2025, 46(3): 574-587.

You, S., Liao, Q., Yue, Y., et al. Enhancing fracture geometry monitoring in hydraulic fracturing using radial basis functions and distributed acoustic sensing. Advances in Geo-Energy Research, 2025, 16(3): 260-275.

Zhan, W., Pu, L., Lei, S., et al. Meshless generalized finite difference method for gas-water two-phase flow equation of complex-shape shale gas reservoirs. Presented at International Conference on Computational & Experimental Engineering and Sciences, 2023: 571-581.

Zhang, D., Wu, H., Jiang, F., et al. Development of coupled fluid-flow/geomechanics model considering storage and transport mechanism in shale gas reservoirs with complex fracture morphology. Scientific Reports, 2024, 14(1): 19238.

Zhang, D., Zhang, L., Tang, H., et al. Fully coupled fluid-solid productivity numerical simulation of multistage fractured horizontal well in tight oil reservoirs. Petroleum Exploration and Development, 2022, 49(2): 382-393.

Zhang, T., Liu, Z., Xie, Z., et al. Numerical simulation of oil shale *in-situ* mining using fluid-thermo-solid coupling. Global Geology, 2020, 23(4): 247-254.

Zhu, M., Ming, P., Xuan, L., et al. An unstructured finite volume time domain method for structural dynamics. Applied Mathematical Modelling, 2012, 36(1): 183-192.